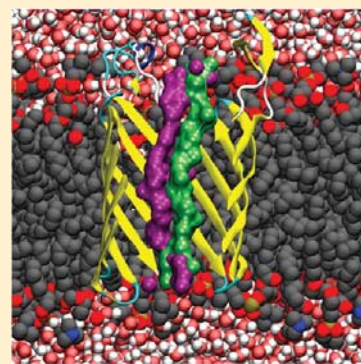


# Ion Permeation in the NanC Porin from *Escherichia coli*: Free Energy Calculations along Pathways Identified by Coarse-Grain Simulations

Jens Dreyer,<sup>†</sup> Paul Strodel,<sup>†</sup> Emiliano Ippoliti,<sup>†</sup> Justin Finnerty,<sup>†</sup> Bob Eisenberg,<sup>‡</sup> and Paolo Carloni<sup>\*,†,§</sup><sup>†</sup>Computational Biophysics, German Research School for Simulation Sciences, D-52425 Jülich, Germany<sup>‡</sup>Department of Molecular Biophysics and Physiology, Rush University Medical Center, Chicago, Illinois 60612, United States<sup>§</sup>Computational Biomedicine, Institute for Advanced Simulations IAS-5, Forschungszentrum Jülich, D-52425 Jülich, Germany

## Supporting Information

**ABSTRACT:** Using the X-ray structure of a recently discovered bacterial protein, the *N*-acetylneuraminic acid-inducible channel (NanC), we investigate computationally  $K^+$  and  $Cl^-$  ions' permeation. We identify ion permeation pathways that are likely to be populated using coarse-grain Monte Carlo simulations. Next, we use these pathways as reaction coordinates for umbrella sampling-based free energy simulations. We find distinct tubelike pathways connecting specific binding sites for  $K^+$  and, more pronounced, for  $Cl^-$  ions. Both ions permeate the porin preserving almost all of their first hydration shell. The calculated free energy barriers are  $G^\ddagger \approx 4$  kJ/mol and  $G^\ddagger \approx 8$  kJ/mol for  $Cl^-$  and  $K^+$ , respectively. Within the approximations associated with these values, discussed in detail in this work, we suggest that the porin is slightly selective for  $Cl^-$  versus  $K^+$ . Our suggestion is consistent with the experimentally observed weak  $Cl^-$  over  $K^+$  selectivity. A rationale for the latter is suggested by a comparison with previous calculations on strongly anion selective porins.



## 1. INTRODUCTION

Bacterial porins are pore-forming, water-filled  $\beta$ -barrel-containing membrane proteins (Chart 1). They allow ions and hydrophilic molecules to cross the outer membrane of gram-negative bacteria and some gram-positive bacteria.<sup>1–4</sup> Their  $\beta$ -barrels are formed by 8–24 strands with largely varying outer diameters of about 2.5–6 nm.<sup>5</sup> The  $\beta$  strands are connected by  $\beta$  turns and long loops in the periplasmic and exoplasmic vestibules, respectively (PV and EV in Chart 1). The  $\beta$ -barrel spans the transmembrane region (TMR).

The permeation of monovalent ions such as  $K^+$  and  $Cl^-$  in porins is of interest. It plays a physiological role in bacteria. In addition, porins predate eukaryotic ion channels in evolution: one may thus expect that features of ion permeation of these bioions are reflected in higher organisms. Hence, microscopic insights into permeation mechanisms in porins may help in the understanding of ion channels as well. These insights mostly come from free energy calculations of ion permeation as a function of a specific reaction coordinate (RC) (or potential of mean force, PMF).<sup>6–19</sup> These are calculated from ion densities obtained by Brownian dynamics,<sup>6,7,10,17</sup> or all-atom molecular dynamics (MD),<sup>7,11–13,17,18</sup> in which the RC is the porin axis (Chart 1). Alternatively, umbrella sampling based on MD<sup>8,9,15,16</sup> or adaptive biasing force<sup>14,19</sup> typically uses the ion position along the porin axis for defining initial configurations for each window (see Table 1). It has been found that (i) the net protein electrostatic potential, in particular in the EV, PV regions, imposes a barrier for entering the lumen for either cations or anions<sup>11,12,14</sup> and (ii) local electrostatic interactions with protein residue side chains,<sup>6–9,11,12,14,17–20</sup> volume

exclusion effects,<sup>11,14,19</sup> ion hydration,<sup>9</sup> and the presence of counterions in the lumen of the porin (Chart 1b)<sup>6,20</sup> play a role for ion permeation.

Multiscale analysis is a useful approach when considering a system like an ion channel that uses atomic scale structures to control macroscopic flows, concentrations, and behavior. It addresses convergence and sampling problems in an efficient manner. Here we use the simplest multiscale approach, a biscale one. We choose as our macroscopic model one that is inherently robust and well-defined because it is the result of fully converged Monte Carlo simulations that predict properties of a range of ion channels (although our particular channel has not been studied by this or any other macroscopic method we know of).

We calculate the umbrella sampling PMF associated with the permeation of  $K^+$  and  $Cl^-$  ions through the *N*-acetylneuraminic acid-conducting (*N*-acetylneuraminic acid is a carbon- and nitrogen-rich nutrient for bacteria) (NanC) porin (we consider here the monomeric form of this porin, which is fully functional) in the outer membrane of *E. coli*.<sup>21</sup> As already reported for other porins,<sup>8,9</sup> we embed the NanC protein into a membrane, here 1,2-dioleoyl-*sn*-glycero-3-phosphocholine (DOPC), surrounded by a water box.

We use an educated guess for the RCs based on a coarse-grain model. Indeed, RCs derived from pathways likely to be largely populated by  $K^+$  or  $Cl^-$  ions along the porin pore. These

Received: August 15, 2013

Revised: October 3, 2013

Chart 1

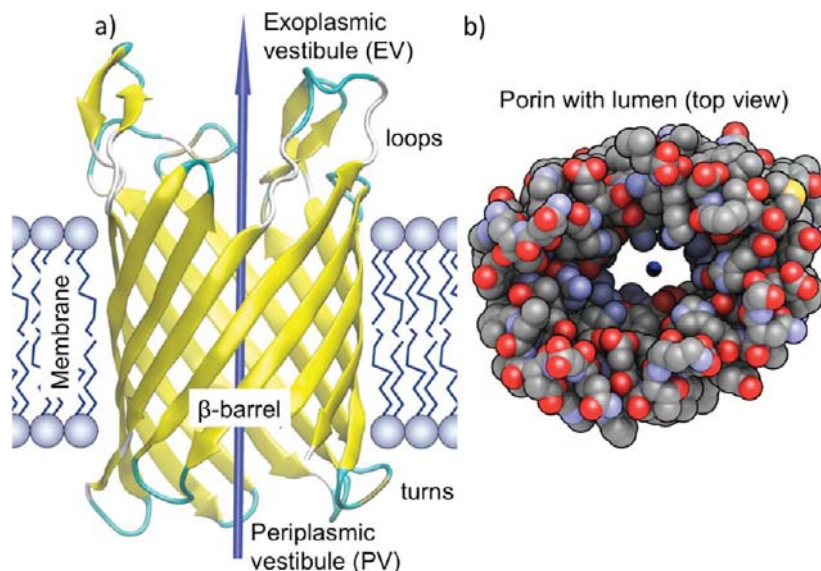


**Table 1. Free Energy Simulations of  $K^+$ ,  $Cl^-$  Permeation (in Italics), or  $Cl^-$  Permeation (in Roman Characters) through Biological and Biomimetic Porins Reported so Far<sup>a</sup>**

protein	method <sup>b</sup>	environment	reaction coord	simulation time (ns)	ref
<i>OmpF</i>	BD	dielectric ( $\epsilon = 2$ )	<i>porin axis</i>	5	6
	MD	DMPC membrane	<i>porin axis</i>	10	7
<i>OprP</i>	ABF	POPE membrane	<i>ion z position</i>	160	14,
<i>OmpC</i>	MD	POPE membrane	<i>porin axis</i>	10	7
<i>human VDAC1</i>	BD	dielectric ( $\epsilon = 2$ )	<i>porin axis</i>		10
<i>human VDAC1</i>	MD	DOPE/DOPC membrane	<i>porin axis</i>	65	11
<i>mouse VDAC1</i>	MD	POPE membrane	<i>porin axis</i>	50	12
	MD, BD	POPE membrane	<i>porin axis</i>	150	17
(14,14) carbon nanotube	UmS	DOPC	<i>ion z position</i>	100	16
<i>Omp32</i>	UmS	electrolyte solution	<i>ion z position</i>	4.5	8
<i>OprP</i>	UmS	DMPC membrane	<i>ion z position</i>	226	9
<i>PorB</i>	MD	DMPC membrane	<i>porin axis</i>	100	13
	MD	DMPC membrane	<i>ion x, z position</i>	100	18
model nanopores	UmS	mimetic membrane ( $CH_4$ )	<i>ion z position</i>	190, 285, 665	15

<sup>a</sup>For MD, umbrella sampling, and ABF calculations, the overall simulation time is reported. <sup>b</sup>BD = Brownian dynamics, MD = molecular dynamics, UmS = umbrella sampling based on MD, ABF = adaptive biasing force.

pathways are derived from population profiles obtained from coarse-grain simulations employing the charge space competition (CSC) models of Nonner and Eisenberg.<sup>22–30</sup> The CSC models explicitly calculate the electrostatic interactions at the expense of full atomistic detail. They represent the ion channel protein as a thick-walled tube with rounded edges. These simplifications to the geometry allow the CSC model Hamiltonian to solve the Poisson equation directly when computing the electrostatic interactions ( $U_{IC}$ ) between the induced charge on the protein–water dielectric boundary and all charged ions (in a computationally efficient manner). These coarse-grain simulations were carried out as described in our previous work.<sup>31</sup> Then, we performed all-atom umbrella sampling simulations of  $K^+$  and  $Cl^-$  ions along their correspondent CSC-derived pathways.

Anticipating our results, we find that the  $Cl^-$  pathway proceeds essentially along a track of electropositive arginine and lysine and a few polar residues on one side of the inner pore, whereas the  $K^+$  pathway passes by electronegative residues that line up on either side of the pore. In addition, our calculated

free energy barrier of  $Cl^-$  is slightly lower (few kJ/mol) than that for  $K^+$ . Despite several approximations which affect the accuracy of our calculations, discussed in detail below, these results are consistent with the weak experimentally observed  $Cl^-$  over  $K^+$  selectivity of the porin.<sup>21,32</sup>

## 2. METHODS

**Theory of the Charge Space Competition Model.** The Hamiltonian for the CSC model is

$$\mathcal{H} = U_C + U_{IC} + U_{mob} + U_{cp} + U_{overlap}$$

where  $U_C$  is the pairwise Coulomb interaction between particles,  $U_{IC}$  is the dielectric boundary potential calculated using the IC discretized integral method<sup>34</sup> (default permittivity values are  $\epsilon_{water} = 80$  and  $\epsilon_{protein} = 10$ ),  $U_{mob}$ <sup>31</sup> is the harmonic potential imposed on the side-chain ions of the SF to generate a population closely matching the X-ray structure,  $U_{cp}$  is the change in chemical potential and change in pressure associated with adding, removing or changing the hydration state of a

particle, and  $U_{\text{overlap}}$  is the potential that avoids overlap of objects in the system. The  $U_{\text{mob}}$  potential reproduces the protein ions' restricted flexibility in a manner analogous to Yu et al.<sup>35</sup>

**Computational Details.** The functional form of the NanC porin is a monomer.<sup>33</sup> The starting structure used for all-atom simulations was based on an X-ray structure at 1.8 Å resolution (PDB code 2WJR).<sup>33</sup> The loop L2, located in EV, is missing in the structure. Here it was added using MODELER<sup>36</sup> (see Supporting Information (SI) for details). A posteriori, we notice that L2 is not involved in the rate-determining steps of ion permeation. Thus, inaccuracies in modeling L2 are not expected to alter the main conclusions of this study. The orientation and coordinates of the porin with respect to the membrane were determined using the OPM server.<sup>37</sup>

Protonation states of NanC ionizable residues were identified through  $pK_a$  predictions using the H++<sup>38</sup> and the PROPKA<sup>39</sup> web servers, as well as MD simulations (see Supporting Information). The resulting protomer, hydrogenated with GROMACS tools, was inserted into a 1,2-dioleoyl-*sn*-glycero-3-phosphocholine (DOPC) membrane/water<sup>40,41</sup> simulation box using the *g\_embed*<sup>42</sup> procedure. Water molecules were added into the protein lumen (Chart 1b) and to the bulk. Bulk water molecules were substituted by ions to generate a neutral 1.5 M electrolyte solution. Note that concentrations of this magnitude are frequently chosen in simulations of electrolytes and used routinely in electrophysiological experiments to study ion permeation.<sup>12</sup> For NanC in particular, reproducible experimental measurements of conductance exist up to 3 M KCl solutions.<sup>32</sup> Care was taken in the choice of the ion and water force fields in order (i) to avoid artifacts like ion crowding found for some force fields<sup>43,44</sup> and (ii) to make sure that the chosen force fields agree well with experimental values for KCl solutions at this concentration. This is true for the parameter set we chose (see below) up to at least 2 M, as demonstrated earlier by our group.<sup>45</sup> The simulation system consists of the protein monomer embedded in a membrane layer of 254 DOPC molecules with ca. 16 000 water molecules and about 1000 ions.

We used the AMBER99SB-ILDN force field<sup>46</sup> for NanC, the GAFF-based force field<sup>47</sup> for DOPC lipids, the TIP3P<sup>48</sup> model for water, and the parameters by Joung and Cheatham<sup>49</sup> for  $K^+$  and  $Cl^-$  ions. Periodic boundary conditions were applied and the particle-mesh Ewald scheme<sup>50</sup> was employed to include long-range interactions with short-range cutoffs of 1.2 nm and a Fourier spacing of 0.1 nm. Constant temperature and pressure conditions were achieved by coupling the system with a Nosé–Hoover thermostat<sup>51,52</sup> and the semi-isotropic Rahman–Parrinello barostat,<sup>53</sup> respectively. 0.1  $\mu$ s MD simulations in the NPT ensemble were carried out (see Supporting Information for more details).

Umbrella sampling<sup>54–56</sup> was used to determine free energies for  $Cl^-$  and  $K^+$  ion permeation with 148 umbrella windows and 2.0 ns of MD simulation per window, in total 296 ns for each ion. The umbrella windows were defined with a spacing of 0.05 nm spanning the  $z$  range from 1.325 to 8.675 nm. Force constants of 2000 kJ/(mol  $\times$  nm<sup>2</sup>) and 1000 kJ/(mol  $\times$  nm<sup>2</sup>) were used in the  $K^+$  and  $Cl^-$  ion calculations, respectively, to restrain the RC. For defining initial positions of the ions for each umbrella window, we followed a two-step procedure. First, a tentative ion permeation pathway was determined from results of coarse-grain simulations using the CSC model.<sup>31</sup> Within this approach the interaction of the KCl solution with

the structural ions of the NanC porin, taking their positions from the X-ray structure,<sup>33</sup> was modeled (see Supporting Information). The concentrations of the KCl solutions in the coarse-grain CSC calculations were 0.22, 0.11, and 0.055 M. The coarse-grain pathway was defined by the points of maximum ion density in cross sections every 0.1 nm along the  $z$ -axis. Second, initial positions were chosen for each umbrella sampling window from the last 5 ns of the NPT MD simulation by choosing configurations for which the ion under investigation exhibits the lowest root-mean-square deviation from the coarse-grain pathway (see Supporting Information). This predefined pathway is used as RC in subsequent umbrella sampling simulations.

Free energy curves were reconstructed from the umbrella sampling data by weighted histogram analysis applying the *g\_wham* procedure<sup>57</sup> with periodicity using the last 1.5 ns of 2.0 ns dynamics in each window. The periodicity options account for the use of a reaction coordinate in a simulation box with periodic boundary conditions. It renders the free energy values on both sides of the porin/membrane system equal.<sup>57</sup> Ion permeation pathways from umbrella sampling were obtained by defining average positions of the permeating ion along the pore, i.e., in each window, by averaging the position of the ions restrained in umbrella sampling over the last 1.5 ns of the 2 ns trajectories.

Water coordination numbers (CN) were determined from the cumulative number radial distribution functions (rdf) of the single permeating as well as all  $K^+$  or  $Cl^-$  ion(s) with respect to water oxygen atoms ( $O_w$ ). Distance cutoffs of 0.362 and 0.385 nm were used for  $K^+$  and  $Cl^-$ , respectively, corresponding to the first minimum in the rdf as determined by Joung and Cheatham applying the ion and water parameters as used here (Table S2 in the SI).<sup>58</sup> Distance analyses were performed using the *g\_mindist* tool of the GROMACS package and averaged over the last 1.5 ns of the trajectory for each umbrella sampling window.

The GROMACS package<sup>59,60</sup> (version 4.5.5) was used for all the simulations. The umbrella sampling routines employed here were introduced in GROMACS through the PLUMED plugin.<sup>61</sup>

### 3. RESULTS

**Molecular Dynamics.** The protein, here embedded in a DOPC bilayer, underwent 100 ns long MD simulation. The density of  $Cl^-$  ions next to track 1 residues (track 1: K153, K111, R85, R129, R107, R105, K91, R72, and K64 spanning the entire pore from the EV to the PV<sup>33</sup>) is larger than that in the opposite region, i.e., close to track 2 residues (track 2: R10, R208, R6, R19, K21 extending from EV to the center of TMR<sup>33</sup>) (see Figure 1c). This is to be expected, as track 1 residues form a strong electropositive region, while track 2 residues are located in a slightly negative electrostatic potential region (Figure 1c). The density of  $K^+$  ions is localized close to polar and negatively charged residues (track 3) (track 3: D154, D132, D148, D188, D4, E204, E17, E186), which alternate with track 2 residues (Figure 1d). At 1.5 M, on average, 1.5  $Cl^-$  ions occupy the PV, 2.6 the TMR, and 1.4 the EV. At the same time, 1.2  $K^+$  ions are on average present in the PV, 2.0 in the TMR, and 1.8 in the EV. Thus, 5.5  $Cl^-$  and 5.0  $K^+$  ions occupy the entire porin on average, consistent with the weak anion selectivity of NanC.<sup>32</sup>

**Free Energy Calculations.** The free energies of  $Cl^-$  and  $K^+$  permeation were calculated using as RCs the CSC maximum

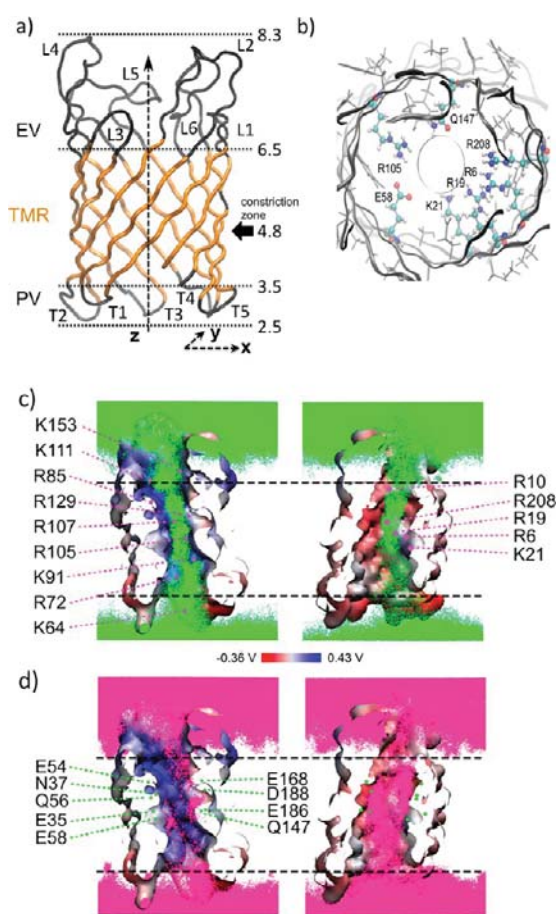


**Figure 1.** (a) Side view of the NanC porin structure (PDB code 2WJR).<sup>33</sup> The protein is a 12-stranded, 2.8 nm high  $\beta$ -barrel.<sup>33</sup> The strands of the transmembrane  $\beta$ -barrel are connected by loops (L1 to L6) in the EV and by turns (T1 to T5) in the PV (panel a). The tube representation of the  $C_{\alpha}$  backbone atoms shows that NanC shares the same architecture of the other porins, sketched in Chart 1.<sup>33</sup> Side chains point into the pore, reducing the average diameter to about 0.66 nm (panel b).<sup>32,33</sup> None of the loops occludes the pore (panel b),<sup>33</sup> different from several other porins.<sup>5</sup> Dashed lines separate different regions of the porin. The porin extends from  $z \approx 2.5$  nm (PV) to  $z \approx 8.3$  nm (EV). The PV itself is located in between  $z \approx 2.5$  nm and  $z \approx 3.5$  nm. The TMR extends from  $z \approx 3.5$  nm to  $z \approx 6.5$  nm, and the EV from  $z \approx 6.5$  nm to  $z \approx 8.3$  nm (panel a). The constriction zone is located at  $z \approx 4.8$  nm (cf. Figure S13 in the Supporting Information (SI)). The DOPC membrane ranges from  $z \approx 2.6$  nm to  $z \approx 7.6$  nm. (b) Lateral view of the same system as (a). TMR side chains pointing toward the pore, which is filled with water molecules (not shown). NanC residues in the constriction zone ( $4.8 \text{ nm} < z < 5.2 \text{ nm}$ ) are indicated using a colored ball-and-stick representation, whereas other side chain heavy atom bonds are shown as gray sticks. The narrowest pore radius is represented as a circle. It has a diameter of 0.54 nm in the crystal structure (Figure S12 in the SI).<sup>33</sup> (c,d) Electrostatic potential projected on the inner pore's van der Waals surface of NanC (cut in two opposing half-cylinders) and averaged over our MD simulation of the protein in KCl solution. The picture includes (c) track 1 (K153 to K64) and track 2 (R10 to K21) positively charged residues (facing each other on opposite sides of the pore) as defined by Wirth et al.<sup>33</sup> as well as  $\text{Cl}^{-}$  ions, represented as green balls. (d) Polar and negatively charged residues (E54 to E58 and E168 to Q147), along with  $\text{K}^{+}$  ions represented as magenta balls.

probability pathways for each of these ions. The RCs that define initial ion positions for each umbrella sampling window are shown in Figure 2 (see also Figure S6 in the SI). The CSC

pathways were found to be essentially concentration independent for the concentration range from 0.055 to 0.22 M studied here, even though the free energy changes quantitatively (Figure S3 in the SI). Both the  $\text{Cl}^{-}$  and  $\text{K}^{+}$  ion densities are distributed across the region between the tracks of positive residues in the porin, where the two tracks exist together, rather than localizing on one positive track or the other. Not surprisingly, the  $\text{Cl}^{-}$  density is displaced toward the electropositive residues in the TMR next to PV, whereas the  $\text{K}^{+}$  density is away from them (Figure 2). The pathways are displaced from the porin axis (see Chart 1 and Figure 1a) by  $\approx 0.1$  nm up to  $\approx 0.6$  nm in the two different regions (Figure S5 in the SI). The free energies were calculated through umbrella sampling, dividing the 7.35 nm long pathway in 148 equally spaced windows along the coarse-grain pathway. Each window was sampled for 2 ns. The free energy minima and transition states are indicated here by  $G_{\text{min}}$  and  $G^{\#}$ , respectively.

**$\text{Cl}^{-}$  Permeation.** The  $\text{Cl}^{-}$  anion enters the EV from the bulk electrolyte solution without a free energy barrier ( $z > 8.3$  nm, Figure 3a). It encounters a small barrier at  $z \approx 7$  nm inside the EV region ( $G^{\#} \approx 3$  kJ/mol) (free energy values are given relative to the bulk as reference value (0 kJ/mol)). It is surrounded by waters almost as in the bulk: its average coordination number is  $\text{CN}_{\text{av}} \approx 6.9$ – $7.0$  as compared to a value of  $\approx 7.1$  in bulk water (Figure 3b).

At the transition from the EV to the TMR, the  $\text{Cl}^{-}$  ion is stabilized in narrow low free energy regions or binding sites ( $z \approx 6.5$  nm,  $G_{\text{min}} \approx 0$  kJ/mol;  $z \approx 6.3$  nm,  $G_{\text{min}} \approx -1$  kJ/mol). At  $z \approx 6.5$  nm the electropositive track 1 residues K111 and K153, along with the polar residue N82 are (on average) the closest residues to the  $\text{Cl}^{-}$  ion (Figure S17 in the SI). The free energy minimum at  $z \approx 6.3$  nm is the lowest. Here, R85, K111, and H78 residues form a binding site (Figure S17), the effective pore radius is relatively small (Figure S13 in the SI), and  $\text{CN}_{\text{av}}$  is reduced to  $\approx 6.4$ .

The pathway along the TMR features several low free energy barriers. The first occurs at  $z \approx 6.0$  nm ( $G^{\#} \approx 2$  kJ/mol). At  $z \approx 5.7$  nm, R85, R107, and R129 (from track 1), along with Q56 and L76, provide stabilizing interactions ( $G_{\text{min}} \approx -1$  kJ/mol). Here,  $\text{CN}_{\text{av}}$  reaches its lowest value ( $\approx 6$ ). After another barrier at  $z \approx 5.4$  nm ( $G^{\#} \approx 2$  kJ/mol), the next free energy minimum occurs at  $z \approx 5.2$  nm ( $G_{\text{min}} \approx 0$  kJ/mol). Here, Q147 and the track 1's R105, R129, and R105 stabilize the anion (Figure S17).  $\text{CN}_{\text{av}}$  is  $\approx 6.3$ . Next, the center of TMR ( $z \approx 4.8$ – $4.9$  nm) features a free energy barrier of  $G^{\#} \approx 3$  kJ/mol, followed by another free energy minimum at  $z \approx 4.6$  nm ( $G_{\text{min}} \approx 1$  kJ/mol).  $\text{Cl}^{-}$  ions are stabilized by track 1 residues K91 and R72, as well as R105 (Figure S17). The smallest effective pore radius is found at  $z \approx 4.8$ – $4.9$  nm (Figure S13) with  $\text{CN}_{\text{av}} \approx 6.4$ . The highest and thus rate-determining free energy barrier of the PMF extends from  $z \approx 4.5$  to  $2.6$  nm. It covers the TMR to PV transition area, with the maximum at  $z \approx 3.3$  nm in the PV ( $G^{\#} \approx 4$  kJ/mol). In this region, stabilizing electropositive residues are lacking. The closest one, at  $\approx 0.9$  nm distance, is K64.  $\text{CN}_{\text{av}}$  increases to  $\approx 6.7$ – $6.8$ . A shallow local minimum in this high-energy region is located at  $z \approx 3.7$  nm in the TMR next to PV ( $G_{\text{min}} \approx 3$  kJ/mol). The  $\text{Cl}^{-}$  ion experiences some stabilization from H137, Q174, and H176, which are anyway rather far from it ( $\approx 0.6$  nm).

**$\text{K}^{+}$  Permeation.** The  $\text{K}^{+}$  cation enters the EV without a barrier ( $z > 8.3$  nm, Figure 3a). Upon passing the EV it experiences a continuous increase in free energy. The average water  $\text{CN}_{\text{av}}$  decreases from the bulk value of  $\approx 6.5$  to  $\approx 5.8$

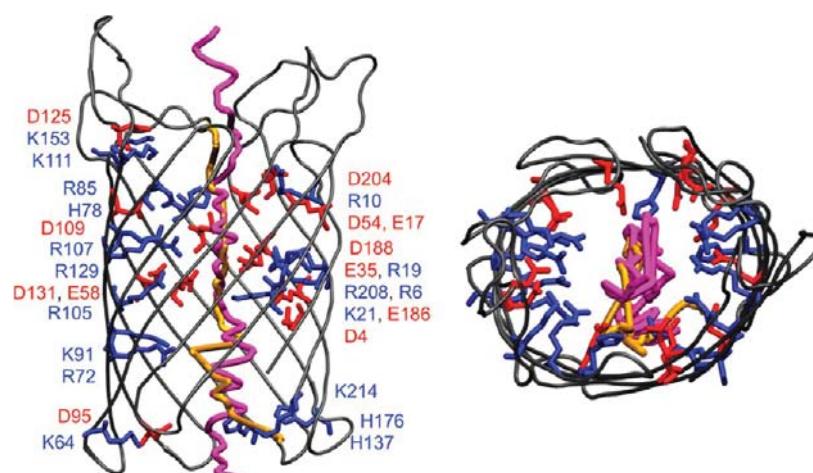


**Figure 2.** Coarse-grain CSC pathways in tube representation for  $\text{Cl}^-$  (yellow) and  $\text{K}^+$  (magenta) permeation in the NanC porin (gray). Residues considered in the coarse-grain CSC simulations are represented as rods for electropositive (blue) and electronegative (red) residues.<sup>31</sup>

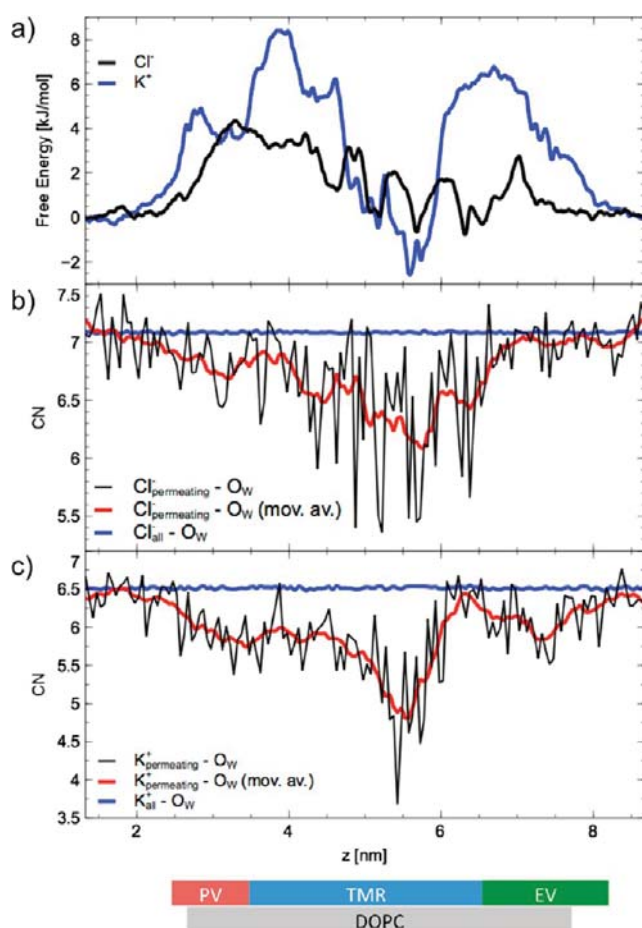


**Figure 3.**  $\text{Cl}^-$  and  $\text{K}^+$  permeation. (a) Free energy as a function of the coordinate  $z$  obtained from umbrella sampling. (b) Coordination number (CN) of the permeating  $\text{Cl}^-$  ion coordinated by water oxygen atoms ( $\text{O}_W$ ) (black line), moving average  $\text{CN}_{\text{av}}$  (red line) and CN of all  $\text{Cl}^-$  ions (blue line). (c) same as (b) for  $\text{K}^+$ .

(Figure 3c). At the transition from the EV to the TMR, the  $\text{K}^+$  cation reaches a broad local maximum at  $z \approx 6.7$  nm ( $G^\ddagger \approx 7$  kJ/mol) with  $\text{CN}_{\text{av}} \approx 5.8$ .

The TMR features a low free energy region with several shallow local minima between  $z \approx 5.7$  and  $z \approx 4.8$  nm. These

constitute the central part of TMR. The first occurs at  $z \approx 5.7$  nm, where D54, E35, and H78 stabilize  $\text{K}^+$  ions ( $G_{\text{min}} \approx -2$  kJ/mol) (Figure S18 in the SI). The lowest free energy ( $G_{\text{min}} \approx -3$  kJ/mol) is then reached at  $z \approx 5.6$  nm. Here,  $\text{CN}_{\text{av}}$  decreases to its lowest value ( $\approx 4.7$ ). Track 3 residues E168 and D188 interact with the cation. Track 2 residues R208 and R6 as well as L190, A170, and S206 are close to this site as well (Figure S18). Next, at  $z \approx 5.2$  nm ( $G_{\text{min}} \approx -1$  kJ/mol) Q147 is the polar residue closest to the ions. D188 (track 3) and the track 2 residues R208 and R6 also contribute to this binding site (Figure S18). The arrangement at the neighboring local minimum at  $z \approx 5.0$  nm ( $G_{\text{min}} \approx 0$  kJ/mol) is similar to the one at  $z \approx 5.2$  nm, except that E168 contributes to stabilize  $\text{K}^+$ . At  $z \approx 4.8$  nm ( $G_{\text{min}} \approx +1$  kJ/mol) Q147, V172, Y133, and A170, as well as E186 (from track 3), form another binding site.

In the TMR toward PV the free energy increases again. First, it reaches a local maximum at  $z \approx 4.6$  nm ( $G^\ddagger \approx 6$  kJ/mol), followed by a local minimum at  $z \approx 4.4$  nm ( $G_{\text{min}} \approx 5$  kJ/mol). Quite distant residues (Y133, K91, A145, V172, and Q174), at  $\approx 0.6$  nm or more, weakly stabilize the cation. At  $z \approx 3.9$  nm, the absolute maximum ( $G^\ddagger \approx 8$  kJ/mol) is characterized by a lack of nearby stabilizing residues.  $\text{CN}_{\text{av}}$  increases to  $\approx 5.9$ .

Upon reaching PV, the free energy decreases to local minima at  $z \approx 3.3$  ( $G_{\text{min}} \approx 4$  kJ/mol) and  $z \approx 3.1$  nm ( $G_{\text{min}} \approx 3$  kJ/mol). Here, the  $\text{K}^+$  ion is weakly stabilized by residues D95 or Q27, respectively, which are relatively far (at  $\approx 0.6$  nm). A local maximum ( $G^\ddagger \approx 5$  kJ/mol) follows at the end of the PV region at  $z \approx 2.8$  nm. Then, the free energy decreases to the bulk water level.  $\text{CN}_{\text{av}}$  increases to its bulk value of  $\approx 6.5$ .

#### 4. DISCUSSION

We have presented MD simulations and PMF calculations based on umbrella sampling for the permeation of  $\text{Cl}^-$  and  $\text{K}^+$  through NanC. This porin was embedded in a DOPC lipid bilayer in the presence of KCl electrolyte solution. The calculations are based on the recently reported X-ray structure.<sup>33</sup>

During the MD, (i) the H-bond network turned out to be similar to that of the X-ray structure (Figure S2–S5 in the SI). The  $\beta$ -barrel core structure forming the TMR is well maintained along the trajectory (average rmsd = 0.19 nm). These values are in line with MD simulations on the structurally similar NaIP porin,<sup>63</sup> where simulations on a 7 ns

time scale showed that the barrel  $C\alpha$  atoms of NaIP exhibited an rmsd of 0.27 nm relative to the X-ray structure.<sup>63</sup> (ii) The quadrupole formed by track 1 and track 2 positively charged residues and track 3 negatively charged residues, pointed out in the X-ray studies of this protein,<sup>33</sup> is maintained. A similar quadrupole has been observed in the OmpG porin X-ray structure.<sup>64</sup> OmpF and OmpC porins instead exhibit a dipolar arrangement of their charged residue groups.<sup>7</sup> (iii) The largest density of  $\text{Cl}^-$  ions is located mostly on the electropositive track 1 (Figures 1c, 4, and 5), whereas that of  $\text{K}^+$  is closer to the

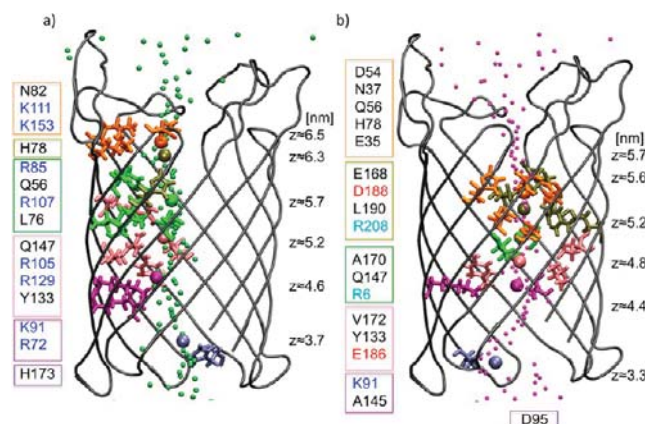


**Figure 4.**  $\text{Cl}^-$  (a) and  $\text{K}^+$  (b) binding sites (free energy minima) emerging from our free energy calculations. Large spheres in different colors denote the ions at their binding sites, and smaller spheres show average ion position in each umbrella sampling window. The NanC structure is represented in tubes connecting the  $C\alpha$  atoms (gray). The binding sites are represented as rods. Their  $z$ -coordinate along the porin axis is shown to the right in nanometers. Residue labels in blue denote track 1 residues, those in cyan track 2 electropositive residues, and those in red track 3 electronegative residues.

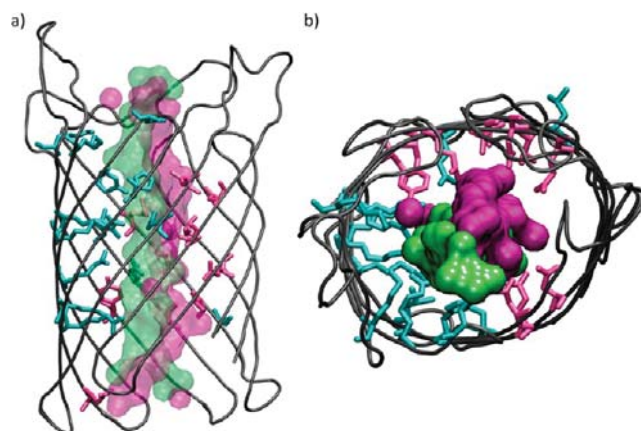


**Figure 5.** (a) Comparison of  $\text{Cl}^-$  (green) and  $\text{K}^+$  (magenta) permeation pathways from umbrella sampling calculations represented as surfaces (see Figure S20 in the SI for a presentation of single pathways): NanC structure in tube representation (gray); important binding sites ( $\text{Cl}^-$  cyan,  $\text{K}^+$  light magenta, cf. Figure 4) from umbrella sampling results are represented as rods. (b) Top view shows ions in the TMR only. (The surface is calculated with the molecular surface solver implemented in VMD<sup>62</sup> using a probe radius of 1.5 Å.)

opposite and neighboring sides of the pore (Figures 1d, 4, and 5). Distinct anion and cation pathways along tracks of electropositive and electronegative residues have also been observed in the MD simulations of OmpF, OmpC in KCl

solution<sup>6,7,20</sup> and those of PorB porin in NaCl<sup>16</sup> or CsCl<sup>13,18</sup> solution, respectively, as well as in umbrella sampling simulations of Omp32<sup>8</sup> and OprP.<sup>9</sup> In OmpF and OmpC, the two pathways show two well-separated screwlike pathways for cations and anions with extended interaction regions.<sup>6,7,20</sup> In Omp32  $\text{Cl}^-$  anions are transported along a basic ladder formed by arginines and lysines.<sup>8</sup> Similarly,  $\text{Cl}^-$  anions almost exclusively pass along a cluster of basic residues on one side of the pore in PorB,<sup>13,18</sup> whereas  $\text{Na}^+$  or  $\text{Cs}^+$  cations move along acidic residues lining up at the opposite wall.<sup>15,16</sup> In contrast, MD and Brownian dynamics studies on mouse VDAC1 porin in KCl solution do not point to defined paths for the  $\text{K}^+$  and  $\text{Cl}^-$  ions.<sup>12,17</sup> Finally, the simulation of the human VDAC1 in KCl solution pointed out that the pathway of  $\text{K}^+$  turned out more restricted than that of  $\text{Cl}^-$ .<sup>11,17</sup>

The PMF calculations were calculated along a pathway identified by coarse-grain CSC calculations.<sup>31</sup> These employ a simplified potential and neglect the full atomistic structure, but allow for extensive sampling in a Monte Carlo sampling procedure. Coarse-grain CSC calculations reveal approximate ion permeation pathways that we subsequently used as input information to umbrella sampling simulations. With this approach, umbrella sampling calculations are performed in regions that are more likely to be relevant for ion permeation through the porin. 148 umbrella sampling windows along the pathways were sampled for as long as 2 ns, and the last 1.5 ns were collected for the analysis presented in the Results section. This is one of the longest umbrella sampling calculation on ion's permeations through porins to date (Table 1).

The  $\text{Cl}^-$  and  $\text{K}^+$  ions retain most of their hydration during permeation, losing, at most,  $\approx 1$  and  $\approx 1.5$  water molecules in the “constriction zone” ( $z \approx 4.8$ , Figure 1a, Figure S13 in the SI). Q56, H78, Q147, and K91 are involved in both ions' binding sites. In addition, arginines (R85, R107, R105, R129, R72) and lysines (K111, K153), along with polar groups N82, H17, and Y133, stabilize the  $\text{Cl}^-$  ions (Figure 4a). Hence, all track 1 electropositive residues except for K64 stabilize the anion. Acidic track 3, D188 and E186, and track 2 residues R208 and R6 are involved in  $\text{K}^+$  binding sites. The binding sites basically coincide with the maxima of ion density as obtained by MD simulation (Figure 1c,d). The ions' permeation pathways obviously line up along the preferential binding sites (Figures 4 and 5). They are confined in the narrow regions of the TMR, whereas in the wider EV and PV regions the average ion positions are more scattered, which may allow for different entry and exit routes to the TMR (Figure S7 in the SI). The pathway for  $\text{Cl}^-$  differs from that of  $\text{K}^+$  (Figures 4 and 5).

The largest free energy barriers of  $\approx 4$  kJ/mol (at  $z \approx 3.3$  nm) and  $\approx 8$  kJ/mol ( $z \approx 3.9$  nm) for  $\text{Cl}^-$  and  $\text{K}^+$ , respectively, are located in the EV to TMR transition area (Figure 3a). They are characterized by the lack of favorable interactions from nearby stabilizing residues accompanied by partial dehydration (both ions are on average dehydrated by less than  $\approx 0.5$  water molecules, Figure 3b,c). Although the errors associated with these values are relatively large (see next section), these results might suggest a weak  $\text{Cl}^-$  over  $\text{K}^+$  selectivity. This suggestion is consistent with experimental evidence.<sup>21,32</sup>

It is interesting to compare with calculations on the strongly anion selective porins Omp32<sup>65,66</sup> and OprP<sup>67</sup> and the moderately anion-selective VDAC1<sup>68–71</sup> porin. Umbrella sampling studies on the Omp32 porin reveal Arg- or Lys-containing single binding sites giving rise to a very positive

potential region in the free energy barrier regions and thus to Omp32's strongly anion selectivity.<sup>8</sup>

Similarly, MD studies on mouse VDAC1 porins suggest that Cl<sup>-</sup> selectivity against K<sup>+</sup> is based on a distribution of Arg and Lys residues, which generates a highly positive electrostatic potential.<sup>12</sup> Previously, adaptive biasing force calculations on OprP<sup>14</sup> pointed to the role of Arg and Lys clusters for Cl<sup>-</sup> selectivity (it should be noted that in OprP phosphate permeation is  $\approx 20$  times higher than Cl<sup>-</sup> transport<sup>67</sup>) against K<sup>+</sup> (in the first two cases, the ions are only slightly dehydrated, while in the latter almost half of the Cl<sup>-</sup> solvation shell is stripped and even more so in case of the K<sup>+</sup> hydrations shell<sup>9,14</sup>), with a particular role of an arginine residue in the OprP center.<sup>19</sup>

In the NanC porin, the presence of Asp and Glu residues close by (within  $\approx 0.6$  nm) to positively charged residues generates only a mildly positive electrostatic potential (Figure 1c,d). This might be an important factor for the small difference of the barriers of K<sup>+</sup> and Cl<sup>-</sup>. Interestingly, MD and Brownian dynamics simulations on human VDAC1<sup>72</sup> suggested a different scenario for the experimentally measured selectivity of Cl<sup>-</sup> versus K<sup>+</sup>. It is proposed that K<sup>+</sup> permeation is slowed down by attractive ion–protein interactions involving Asp and Glu residues in the middle of the pore and that K<sup>+</sup> ions encounter larger free energy barriers for entering the porin.<sup>10,11</sup>

Our calculations further suggest that free energies of both ions may be slightly lower (by less than 3 kJ/mol) than that of bulk water in regions in the TMR (Figure 3a). This has been suggested in a variety of simulations of other porins.<sup>7,10,12,17</sup>

Several local barriers for the permeation are observed (Figure 3a). They range between 1 and 3 kJ/mol for Cl<sup>-</sup> and between 1 and 7 kJ/mol for K<sup>+</sup>. They can all essentially be described by transitions between binding sites, thus by the transient loss of stabilizing interactions. Similar features have been observed also for Omp32<sup>8</sup> and PorB<sup>13,18</sup>

**Accuracy of the PMF Calculations.** Comparing the profiles collected after 0.5 ns for 0.3 to 1.5 ns is used here to investigate the statistical convergence of the results. The PMF of Cl<sup>-</sup> is converged to  $\approx 0.5$  kJ/mol for  $z$  less than  $\approx 2.5$  nm and larger than  $\approx 4.5$  nm, whereas in between  $z \approx 2.5$ – $4.5$  nm deviations of the PMFs amount to a maximum of  $\approx 1$  kJ/mol (Figure S15 in the SI). That of K<sup>+</sup> is converged to  $\approx 0.5$  kJ/mol or less (Figure S16 in the SI). In spite of the good convergence of these calculations, one has to take into account several other errors. These are associated with (i) force fields inaccuracies (especially for K<sup>+</sup> and to a lesser extent Cl<sup>-</sup>);<sup>45,49,73,74</sup> (ii) the use of only one collective variable to describe the permeation process;<sup>75</sup> and (iii) the dependence of the results on the initial structures. Structures fluctuate dramatically when viewed on the time scale of permeation. Permeation and selectivity may occur in a subset of these fluctuating structures, hence affecting the results.

Hence, although cancellation of errors can be present when one considers differences in free energies rather than absolute values, and in spite of the fact that this is one of the longest PMF calculations performed so far on a porin (Table 1), one has to be very careful when drawing conclusions about selectivity, as pointed out in the previous section.

## 5. CONCLUSIONS

We have applied a two-step procedure to ion permeation through wide porins. Coarse-grain modeling is employed to identify pathways, which are subsequently used as reaction

coordinates for all-atom MD simulations. We applied this approach to investigate Cl<sup>-</sup> and K<sup>+</sup> permeation through NanC. We find distinct pathways for both ions. Our calculations might suggest that the free energy barrier for Cl<sup>-</sup> is slightly lower than for K<sup>+</sup>, in agreement with the observed weak Cl<sup>-</sup> over K<sup>+</sup> selectivity.<sup>21,32</sup> In this respect, besides the many approximations discussed above, we further notice that any free energy calculation is a function of all interactions in the system and so is expected to be a sensitive function of the concentration and composition of bathing solutions on either side of the porin as well as of the transmembrane potential. Thus, conclusions of calculations done without a calibrated treatment of mixtures cannot be assumed to be valid in physiological solutions, which are mixtures in which divalent concentrations are so important and gradients of divalent concentrations are so large.<sup>76–80</sup>

## ■ ASSOCIATED CONTENT

### 📄 Supporting Information

Starting structures for the protein and membrane system, protonation state selection, MD simulation setup, coarse-grain charge space competition (CSC) models, analysis of simulations, NanC structural stability and properties, and umbrella sampling analysis. This material is available free of charge via the Internet at <http://pubs.acs.org>.

## ■ AUTHOR INFORMATION

### Notes

The authors declare no competing financial interest.

## ■ ACKNOWLEDGMENTS

Financial funding from the DFG CA 973/1-1 is gratefully acknowledged, as well as computational time on the Jülich JUROPA supercomputing system. We thank the reviewers for their constructive criticism. German Research School for Simulation Sciences is a joint venture of RWTH Aachen University and Forschungszentrum Jülich, Germany.

## ■ REFERENCES

- (1) Schulz, G. Bacterial Porins: Structure and Function. *Curr. Opin. Cell. Biol.* **1993**, *5*, 701–707.
- (2) Delcour, A. Solute Uptake through General Porins. *Front. Biosci.* **2003**, *8*, D1055–D1071.
- (3) Novikova, O.; Solovyeva, T. Non-Specific Porins of the Outer Membrane of Gram-Negative Bacteria: Structure and Functions. *Biochem. (Moscow) Suppl. Ser. A* **2009**, *26*, 6–20.
- (4) Aguilera, V.; Queralt-Martin, M.; Aguilera-Arzo, M.; Alcaraz, A. Insights on the Permeability of Wide Protein Channels: Measurement and Interpretation of Ion Selectivity. *Integr. Biol.* **2011**, *3*, 159–172.
- (5) Fairman, J. W.; Noinaj, N.; Buchanan, S. K. The Structural Biology of Beta-Barrel Membrane Proteins: A Summary of Recent Reports. *Curr. Opin. Struct. Biol.* **2011**, *21*, 523–531.
- (6) Im, W.; Roux, B. Ion Permeation and Selectivity of OmpF Porin: A Theoretical Study Based on Molecular Dynamics, Brownian Dynamics, and Continuum Electrodiffusion Theory. *J. Mol. Biol.* **2002**, *322*, 851–869.
- (7) Biro, I.; Pezeshki, S.; Weingart, H.; Winterhalter, M.; Kleinekathofer, U. Comparing the Temperature-Dependent Conductance of the Two Structurally Similar *E. Coli* Porins Ompc and Ompf. *Biophys. J.* **2010**, *98*, 1830–1839.
- (8) Zachariae, U.; Helms, V.; Engelhardt, H. Multistep Mechanism of Chloride Translocation in a Strongly Anion-Selective Porin Channel. *Biophys. J.* **2003**, *85*, 954–962.
- (9) Pongprayoon, P.; Beckstein, O.; Wee, C.; Sansom, M. Simulations of Anion Transport through OprP Reveal the Molecular

Basis for High Affinity and Selectivity for Phosphate. *Proc. Natl. Acad. Sci. U.S.A.* **2009**, *106*, 21614–21618.

(10) Lee, K.; Rui, H.; Pastor, R.; Im, W. Brownian Dynamics Simulations of Ion Transport through the VDAC. *Biophys. J.* **2011**, *100*, 611–619.

(11) Rui, H.; Lee, K.; Pastor, R.; Im, W. Molecular Dynamics Studies of Ion Permeation in VDAC. *Biophys. J.* **2011**, *100*, 602–610.

(12) Krammer, E.; Homblé, F.; Prévost, M. Concentration Dependent Ion Selectivity in VDAC: A Molecular Dynamics Simulation Study. *PLoS One* **2011**, *6*, e27994.

(13) Kutzner, C.; Grubmüller, H.; de Groot, B. L.; Zachariae, U. Computational Electrophysiology: The Molecular Dynamics of Ion Channel Permeation and Selectivity in Atomistic Detail. *Biophys. J.* **2011**, *101*, 809–817.

(14) Modi, N.; Benz, R.; Hancock, R. E. W.; Kleinekathöfer, U. Modeling the Ion Selectivity of the Phosphate Specific Channel OprP. *J. Phys. Chem. Lett.* **2012**, *3*, 3639–3645.

(15) Pongprayoon, P.; Beckstein, O.; Sansom, M. S. P. Biomimetic Design of a Brush-Like Nanopore: Simulation Studies. *J. Phys. Chem. B* **2012**, *116*, 462–468.

(16) García-Fandiño, R.; Sansom, M. S. P. Designing Biomimetic Pores Based on Carbon Nanotubes. *Proc. Natl. Acad. Sci. U.S.A.* **2012**, *109*, 6939–6944.

(17) Krammer, E.-M.; Homblé, F.; Prévost, M. Molecular Origin of VDAC Selectivity Towards Inorganic Ions: A Combined Molecular and Brownian Dynamics Study. *Biochim. Biophys. Acta (BBA): Biomembranes* **2013**, *1828*, 1284–1292.

(18) Kattner, C.; Zauha, J.; Jaenecke, F.; Zachariae, U.; Tanabe, M. Identification of a Cation Transport Pathway in Neisseria Meningitidis Porb. *Proteins: Struct., Funct. Bioinf.* **2013**, *81*, 830–840.

(19) Modi, N.; Bárcena-Urribarri, I.; Bains, M.; Benz, R.; Hancock, R. E. W.; Kleinekathöfer, U. Role of the Central Arginine R133 toward the Ion Selectivity of the Phosphate Specific Channel OprP: Effects of Charge and Solvation. *Biochemistry* **2013**, *52*, 5522–5532.

(20) Schirmer, T.; Phale, P. Brownian Dynamics Simulation of Ion Flow through Porin Channels. *J. Mol. Biol.* **1999**, *294*, 1159–1167.

(21) Condemine, G.; Berrier, C.; Plumbridge, J.; Ghazi, A. Function and Expression of an N-Acetylneuraminic Acid-Inducible Outer Membrane Channel in Escherichia Coli. *J. Bacteriol.* **2005**, *187*, 1959–1965.

(22) Nonner, W.; Chen, D. P.; Eisenberg, B. Anomalous Mole Fraction Effect, Electrostatics, and Binding in Ionic Channels. *Biophys. J.* **1998**, *74*, 2327–2334.

(23) Nonner, W.; Eisenberg, B. Ion Permeation and Glutamate Residues Linked by Poisson-Nernst-Planck Theory in L-Type Calcium Channels. *Biophys. J.* **1998**, *75*, 1287–1305.

(24) Nonner, W.; Catacuzzeno, L.; Eisenberg, B. Binding and Selectivity in L-Type Calcium Channels: A Mean Spherical Approximation. *Biophys. J.* **2000**, *79*, 1976–1992.

(25) Boda, D.; Busath, D. D.; Henderson, D.; Sokolowski, S. Monte Carlo Simulations of the Mechanism of Channel Selectivity: The Competition between Volume Exclusion and Charge Neutrality. *J. Phys. Chem. B* **2000**, *104*, 8903–8910.

(26) Boda, D.; Henderson, D. D.; Busath, D. D. Monte Carlo Study of the Effect of Ion and Channel Size on the Selectivity of a Model Calcium Channel. *J. Phys. Chem. B* **2001**, *105*, 11574–11577.

(27) Nonner, W.; Gillespie, D.; Henderson, D.; Eisenberg, B. Ion Accumulation in a Biological Calcium Channel: Effects of Solvent and Confining Pressure. *J. Phys. Chem. B* **2001**, *105*, 6427–6436.

(28) Boda, D.; Busath, D.; Eisenberg, B.; Henderson, D.; Nonner, W. Monte Carlo Simulations of Ion Selectivity in a Biological Na<sup>+</sup> Channel: Charge-Space Competition. *Phys. Chem. Chem. Phys.* **2002**, *4*, 5154–5160.

(29) Gillespie, D.; Eisenberg, R. S. Physical Descriptions of Experimental Selectivity Measurements in Ion Channels. *Eur. Biophys. J.* **2002**, *31*, 454–466.

(30) Boda, D.; Gillespie, D.; Nonner, W.; Henderson, D.; Eisenberg, B. Computing Induced Charges in Inhomogeneous Dielectric Media:

Application in a Monte Carlo Simulation of Complex Ionic Systems. *Phys. Rev. E* **2004**, *69*, 046702.

(31) Finnerty, J. J.; Eisenberg, R.; Carloni, P. Localizing the Charged Side Chains of Ion Channels within the Crowded Charge Models. *J. Chem. Theory Comput.* **2013**, *9*, 766–773.

(32) Giri, J.; Tang, J.; Wirth, C.; Peneff, C.; Eisenberg, B. Single-Channel Measurements of an N-Acetylneuraminic Acid-Inducible Outer Membrane Channel in Escherichia Coli. *Eur. Biophys. J.* **2012**, *41*, 259–271.

(33) Wirth, C.; Condemine, G.; Boiteux, C.; Berneche, S.; Schirmer, T.; Peneff, C. Nanc Crystal Structure, a Model for Outer-Membrane Channels of the Acidic Sugar-Specific Kdgm Porin Family. *J. Mol. Biol.* **2009**, *394*, 718–731.

(34) Allen, R.; Hansen, J. P.; Melchionna, S. Electrostatic Potential inside Ionic Solutions Confined by Dielectrics: A Variational Approach. *Phys. Chem. Chem. Phys.* **2001**, *3*, 4177–4186.

(35) Yu, H.; Noskov, S. Y.; Roux, B. Two Mechanisms of Ion Selectivity in Protein Binding Sites. *Proc. Natl. Acad. Sci. U.S.A.* **2010**, *107*, 20329–20334.

(36) Fiser, A.; Šali, A. In *Methods in Enzymology*; Carter, C. W., Jr., Robert, M. S., Eds.; Academic Press: New York, 2003; Vol. 374, pp 461–491.

(37) Lomize, M. A.; Pogozheva, I. D.; Joo, H.; Mosberg, H. I.; Lomize, A. L. Opm Database and Ppm Web Server: Resources for Positioning of Proteins in Membranes. *Nucleic Acids Res.* **2012**, *40*, D370–D376.

(38) Gordon, J.; Myers, J.; Folta, T.; Shoja, V.; Heath, L. S.; Onufriev, A. H<sup>++</sup>: A Server for Estimating pK<sub>a</sub>s and Adding Missing Hydrogens to Macromolecules. *Nucleic Acids Res.* **2005**, *33*, W368–W371.

(39) Bas, D.; Rogers, D.; Jensen, J. Very Fast Prediction and Rationalization of pK<sub>a</sub> Values for Protein-Ligand Complexes. *Proteins: Struct., Funct., Bioinf.* **2008**, *73*, 765–783.

(40) Vácha, R.; Siu, S. W. I.; Petrov, M.; Böckmann, R. A.; Barucha-Kraszewska, J.; Jurkiewicz, P.; Hof, M.; Berkowitz, M. L.; Jungwirth, P. Effects of Alkali Cations and Halide Anions on the Dopc Lipid Membrane. *J. Phys. Chem. A* **2009**, *113*, 7235–7243.

(41) The initial DOPC/water system was provided by the authors of ref 40 for download at <http://marge.uochb.cas.cz/~vacha/download.htm>. The system was replicated into a 2 × 2 supercell.

(42) Wolf, M.; Hoefling, M.; Aponte-Santamaría, C.; Grubmüller, H.; Groenhof, G. g<sub>membed</sub>: Efficient Insertion of a Membrane Protein into an Equilibrated Lipid Bilayer with Minimal Perturbation. *J. Comput. Chem.* **2010**, *31*, 2169–2174.

(43) Auffinger, P.; Cheatham, T.; Vaiana, A. Spontaneous Formation of KCl Aggregates in Biomolecular Simulations: A Force Field Issue? *J. Chem. Theor. Comput.* **2007**, *3*, 1851–1859.

(44) Fennell, C.; Bizjak, A.; Vlachy, V.; Dill, K. Ion Pairing in Molecular Simulations of Aqueous Alkali Halide Solutions. *J. Phys. Chem. B* **2009**, *113*, 6782–6791.

(45) Zhang, C.; Raugei, S.; Eisenberg, B.; Carloni, P. Molecular Dynamics in Physiological Solutions: Force Fields, Alkali Metal Ions, and Ionic Strength. *J. Chem. Theor. Comput.* **2010**, *6*, 2167–2175.

(46) Lindorff-Larsen, K.; Piana, S.; Palmo, K.; Maragakis, P.; Klepeis, J.; Dror, R.; Shaw, D. Improved Side-Chain Torsion Potentials for the Amber Ff99sb Protein Force Field. *Proteins: Struct., Funct., Bioinf.* **2010**, *78*, 1950–1958.

(47) Siu, S.; Vácha, R.; Jungwirth, P.; Böckmann, R. Biomolecular Simulations of Membranes: Physical Properties from Different Force Fields. *J. Chem. Phys.* **2008**, *128*, 125103.

(48) Jorgensen, W. L.; Chandrasekhar, J.; Madura, J. D.; Impey, R. W.; Klein, M. L. Comparison of Simple Potential Functions for Simulating Liquid Water. *J. Chem. Phys.* **1983**, *79*, 926–935.

(49) Joung, I.; Cheatham, T. Determination of Alkali and Halide Monovalent Ion Parameters for Use in Explicitly Solvated Biomolecular Simulations. *J. Phys. Chem. B* **2008**, *112*, 9020–9041.

(50) Essmann, U.; Perera, L.; Berkowitz, M. L.; Darden, T.; Lee, H.; Pedersen, L. G. A Smooth Particle Mesh Ewald Method. *J. Chem. Phys.* **1995**, *103*, 8577–8593.

- (51) Nose, S. A Molecular-Dynamics Method for Simulations in the Canonical Ensemble. *Mol. Phys.* **1984**, *52*, 255–268.
- (52) Hoover, W. G. Canonical Dynamics: Equilibrium Phase-Space Distributions. *Phys. Rev. A* **1985**, *31*, 1695–1697.
- (53) Parrinello, M.; Rahman, A. Polymorphic Transitions in Single-Crystals - a New Molecular-Dynamics Method. *J. Appl. Phys.* **1981**, *52*, 7182–7190.
- (54) Kumar, S.; Rosenberg, J. M.; Bouzida, D.; Swendsen, R. H.; Kollman, P. A. The Weighted Histogram Analysis Method for Free-Energy Calculations on Biomolecules. I. The Method. *J. Comput. Chem.* **1992**, *13*, 1011–1021.
- (55) Torrie, G. M.; Valleau, J. P. Monte Carlo Free Energy Estimates Using Non-Boltzmann Sampling: Application to the Sub-Critical Lennard-Jones Fluid. *Chem. Phys. Lett.* **1974**, *28*, 578–581.
- (56) Kaestner, J. Umbrella Sampling. *Wiley Int. Rev. Comput. Mol. Sci.* **2011**, *1*, 932–942.
- (57) Hub, J.; de Groot, B.; van Der Spoel, D. G\_Wham — a Free Weighted Histogram Analysis Implementation Including Robust Error and Autocorrelation Estimates. *J. Chem. Theor. Comput.* **2010**, *6*, 3713–3720.
- (58) Joung, I. S.; Cheatham, T. E. Molecular Dynamics Simulations of the Dynamic and Energetic Properties of Alkali and Halide Ions Using Water-Model-Specific Ion Parameters. *J. Phys. Chem. B* **2009**, *113*, 13279–13290.
- (59) Lindahl, E.; Hess, B.; van der Spoel, D. Gromacs 3.0: A Package for Molecular Simulation and Trajectory Analysis. *J. Mol. Model.* **2001**, *7*, 306–317.
- (60) Hess, B.; Kutzner, C.; van der Spoel, D.; Lindahl, E. Gromacs 4: Algorithms for Highly Efficient, Load-Balanced, and Scalable Molecular Simulation. *J. Chem. Theory Comput.* **2008**, *4*, 435–447.
- (61) Bonomi, M.; Branduardi, D.; Bussi, G.; Camilloni, C.; Provasi, D.; Raiteri, P.; Donadio, D.; Marinelli, F.; Pietrucci, F.; Broglia, R.; Parrinello, M. Plumed: A Portable Plugin for Free-Energy Calculations with Molecular Dynamics. *Comput. Phys. Commun.* **2009**, *180*, 1961–1972.
- (62) Humphrey, W.; Dalke, A.; Schulten, K. VMD - Visual Molecular Dynamics. *J. Mol. Graph. Model.* **1996**, *14*, 33–38.
- (63) Khalid, S.; Sansom, M. Molecular Dynamics Simulations of a Bacterial Autotransporter: NaIP from *Neisseria Meningitidis*. *Mol. Membr. Biol.* **2006**, *23*, 499–508.
- (64) Yildiz, O.; Vinothkumar, K. R.; Goswami, P.; Kuhlbrandt, W. Structure of the Monomeric Outer-Membrane Porin OmpG in the Open End Closed Conformation. *EMBO J.* **2006**, *25*, 3702–3713.
- (65) Mathes, A.; Engelhardt, H. Nonlinear and Asymmetric Open Channel Characteristics of an Ion-Selective Porin in Planar Membranes. *Biophys. J.* **1998**, *75*, 1255–1262.
- (66) Zachariae, U.; Koumanov, A.; Engelhardt, H.; Karshikoff, A. Electrostatic Properties of the Anion Selective Porin Omp32 from *Delftia Acidovorans* and of the Arginine Cluster of Bacterial Porins. *Protein Sci.* **2002**, *11*, 1309–1319.
- (67) Benz, R.; Egli, C.; Hancock, R. E. W. Anion Transport through the Phosphate-Specific OprP-Channel of the *Pseudomonas Aeruginosa* Outer Membrane: Effects of Phosphate, Di- and Tribasic Anions and of Negatively-Charged Lipids. *Biochim. Biophys. Acta* **1993**, *1149*, 224–230.
- (68) Colombini, M. Structure and Mode of Action of a Voltage Dependent Anionselective Channel (VDAC) Located in the Outer Mitochondrial Membrane. *Ann. N.Y. Acad. Sci.* **1980**, *341*, 552–563.
- (69) Colombini, M. Purification of VDAC (Voltage-Dependent Anion-Selective Channel) from Rat Liver Mitochondria. *J. Membr. Biol.* **1983**, *74*, 115–121.
- (70) Colombini, M. Voltage Gating in the Mitochondrial Channel, VDAC. *J. Membr. Biol.* **1989**, *111*, 103–111.
- (71) Hodge, T.; Colombini, M. Regulation of Metabolite Flux through Voltagegating of VDAC Channels. *J. Membr. Biol.* **1997**, *157*, 271–279.
- (72) Brdiczka, D. In *Molecular Systems Bioenergetics*; Saks, V., Ed.; Wiley-VCH Verlag GmbH & Co. KGaA: Weinheim, Germany, 2007; p 165.
- (73) Joung, I.; Cheatham, T. Molecular Dynamics Simulations of the Dynamic and Energetic Properties of Alkali and Halide Ions Using Water-Model-Specific Ion Parameters. *J. Phys. Chem. B* **2009**, *113*, 13279–13290.
- (74) Yoon, M.; Suh, K.; Kim, H.; Kim, Y.; Selvapalam, N.; Kim, K. High and Highly Anisotropic Proton Conductivity in Organic Molecular Porous Materials. *Ang. Chem. Int. Ed.* **2011**, *123*, 8016–8019.
- (75) Leone, V.; Marinelli, F.; Carloni, P.; Parrinello, M. Targeting Biomolecular Flexibility with Metadynamics. *Curr. Opin. Struct. Biol.* **2010**, *20*, 148–154.
- (76) Gillespie, D. Energetics of Divalent Selectivity in a Calcium Channel: The Ryanodine Receptor Case Study. *Biophys. J.* **2008**, *94*, 1169–1184.
- (77) Eisenberg, B. *Self-Organized Model of Selectivity*; Institute of Mathematics and Its Applications IMA, University of Minnesota: Minneapolis, MN, 2009; <http://arxiv.org/0906.5173>.
- (78) Boda, D.; Giri, J.; Henderson, D.; Eisenberg, B.; Gillespie, D. Analyzing the Components of the Free-Energy Landscape in a Calcium Selective Ion Channel by Widom's Particle Insertion Method. *J. Chem. Phys.* **2011**, *134*, 055102.
- (79) Giri, J.; Fonseca, J.; Boda, D.; Henderson, D.; Eisenberg, B. Self-Organized Models of Selectivity in Calcium Channels. *Phys. Biol.* **2011**, *8*, 026004.
- (80) Burger, M. Inverse Problems in Ion Channel Modelling. *Inverse Problems* **2011**, *27*, 083001.